Modeling the Solar Wind Turbulent Cascade Including Cross Helicity: With and Without Expansion

Roland Grappin[1,2] ⓘ, Andrea Verdini[3,4], and W.-C. Müller[5,6]

[1] Laboratoire de Physique des Plasmas (LPP), École Polytechnique, Rte de Saclay, 91120 Palaiseau, France; roland.grappin@lpp.polytechnique.fr
[2] CNRS, Observatoire de Paris, Sorbonne Université, Université Paris Saclay, Ecole Polytechnique, Institut Polytechnique de Paris, F-91120 Palaiseau, France
[3] Università di Firenze, Dipartimento di Fisica e Astronomia, Firenze, Italy
[4] INAF, OAA, Firenze, Italy
[5] Technische Universität Berlin, ER 3-2, Hardenbergstr. 36a, D-10623 Berlin, Germany
[6] Max-Planck/Princeton Center for Plasma Physics, Hofgartenstr., 8 80539 Munich, Germany/Princeton University P.O. Box 430 Princeton, NJ 08544-1019, USA

Abstract

Simulations of the turbulent cascade forming in the solar wind, including cross helicity, commonly adopt a homogeneous setup, not taking into account wind expansion. Here we want to assess the predictions of decaying 3D compressible (low Mach number) MHD simulations, respectively homogeneous and with expansion, in order to examine which is the most fruitful approach to understanding the turbulent cascade in the solar wind. We follow turbulent evolution during 10 nonlinear turnover times, considering several initial values of the initial spectral slope and cross helicity. In the expanding case, the transverse sizes of the plasma volume are stretched by a factor of 5 during the simulation, corresponding to traveling from 0.2 up to 1 au. In homogeneous simulations, the relative cross helicity rises, and the Elsässer spectra $E_{\pm}$ show "pinning," with a steep dominant spectrum and flat subdominant spectrum, the final spectral indices depending on cross helicity but not initial indices. With expansion, the relative cross helicity decreases, and dominant and subdominant spectra share the same index, with the index relaxing to an asymptotic value that generally depends on the initial index. The absence of pinning, as well as the decrease of relative cross helicity, probably both rely on the permanent injection by expansion of an excess of magnetic energy at the largest scales, equivalent to injecting subdominant energy. Also, spectra generally steepen when initially starting flatter than $k^{-5/3}$ but stop evolving at a finite time/distance.

Unified Astronomy Thesaurus concepts: Interplanetary turbulence (830); Solar wind (1534); Space plasmas (1544); Alfven waves (23); Interplanetary medium (825); Magnetohydrodynamics (1964)

1. Introduction

Turbulent dissipation and heating play an important role in the evolution of the interplanetary plasma and the acceleration of the solar wind, as demonstrated in solar wind models (Cranmer et al. 2007; Verdini et al. 2010; Chandran et al. 2011; van der Holst et al. 2014; Shoda et al. 2018, 2019; Réville et al. 2020; Matsumoto 2021). At the base of this, there is the question of the nature of the turbulent cascade at work in the solar wind.

To proceed, one can compare direct predictions of cascade theories to observations, possibly with the help of direct simulations. A good example is that of local spectral anisotropy, computed in a frame attached to the local mean magnetic field and using structure functions. Assuming axial symmetry around the direction of the local mean field, work by Horbury et al. (2008) first recovered the so-called critical balance results, in which the perpendicular cascade is strong and the spectrum along the mean field is generated by linear transport along it. Later, work by Chen et al. (2012) showed important deviations from axisymmetry around the local mean field. This was reproduced by 3D MHD simulations showing that expansion breaks the local axisymmetry in the whole inertial range (Verdini & Grappin 2015).

A second example is that of the origin of the global spectral anisotropy, that is, the origin of the so-called Maltese cross (Matthaeus et al. 1990) obtained in a frame attached to the mean magnetic field computed during a fixed interval of time. We identified the two branches of the Maltese cross as corresponding to the signature of, respectively, weak or strong expansion. We could reproduce the two configurations via simulations with expansion and in both cases recover the observed slow plasma cooling with distance (Montagud-Camps et al. 2018, 2020). A last interesting example is that of the origin of the switchback formation in the early solar wind, which seems to be possibly attributed to the expansion of the plasma (Squire et al. 2020).

Despite these successes, the large majority of work in which a cascade theory is proposed for the solar wind neglects expansion (e.g., Boldyrev 2005; Lithwick et al. 2007; Perez & Boldyrev 2010; Chandran et al. 2015). These works predict specific spectral scalings for $z_{\pm}$ (see definition below) or velocity and magnetic fluctuations covering the observed range $[-5/3, -3/2]$. However, in situ observations show that the spectral indices, at scales above the sub-ion scale, are distributed in a large interval of values at a given distance (Grappin et al. 1991; Boldyrev et al. 2011), and that the spectral index varies with distance (Bavassano et al. 1982; Chen et al. 2020) and the average properties of the flow, such as proton temperature (Grappin et al. 1991), solar wind speed, and cross helicity (Chen et al. 2013). In this paper, we investigate such properties via numerical simulations, comparing the results obtained with and without expansion and insisting on Alfvénic (i.e., high cross helicity) streams, which are ubiquitous in the solar wind.
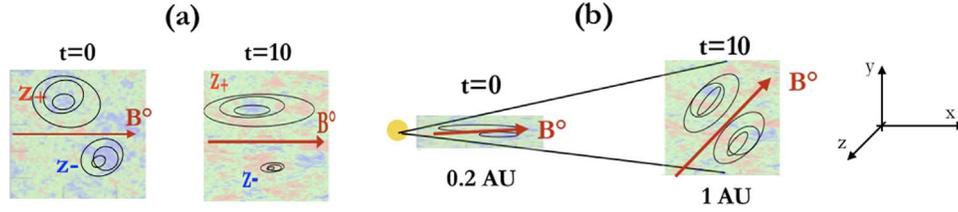
Figure 1. Sketch of the initial and final plasma volumes after 10 nonlinear times in (a) standard homogeneous MHD simulations and (b) simulations with expansion (see text).

Note that a whole family of works dealing with the evolution of turbulence in the solar wind (e.g., Adhikari et al. 2020) does not describe the details of the cascade, such as the evolution of turbulent energy spectra, but instead directly proposes approximate evolution equations for moments, i.e., energies and correlations, including some known properties associated with expansion.

In the present work, we instead follow in detail the formation and decay of the turbulent cascade by solving the primitive MHD equations in two versions: the standard compressive MHD equations (without expansion) on one side and MHD equations with finite expansion on the other side, also called EBM equations (see below). The plasma evolution is followed during 10 nonlinear times, which in the expanding case corresponds to the heliocentric distance of the plasma volume increasing by a factor of 5, e.g., varying from 0.2 to 1 au. We consider in this work cases dominated by outward-propagating Alfvén waves, as well as cases with equal populations propagating in both directions, as both cases are important in the solar wind.

We run weakly compressive simulations, i.e., with a turbulent Mach number equal to 0.12, characteristic of the quasi-incompressible fluctuations at hour scales (Matthaeus et al. 1991; Bavassano & Bruno 1995; Ofman 2010). We adopt in our simulations with expansion an expansion rate $\epsilon = 0.4$ (see definition below; Equation (7)), a value for which expansion terms are comparable to nonlinear terms at the large scales. Such an expansion rate is characteristic of scales of the order of 1 day (Montagud-Camps et al. 2020); a more realistic study would require using a smaller expansion rate and/or a very high resolution in order to include scales smaller than 1 hr, but this would require important numerical resources, and we think that the present choice of parameters is a reasonable compromise for a first study. These choices allow one to study a quasi-incompressible turbulent state and clearly reveal the differences between homogeneous turbulence and turbulence with expansion.

The plan of the present paper is as follows. Section 2 describes the equations, basic parameters, and initial conditions of the simulations. Section 3 gives the results. Section 4 is a discussion, and Section 5 is a conclusion.

2. Method: Equations

2.1. Equations and Definitions

Here we briefly derive the basic equations and method (for a more detailed derivation, see, e.g., Grappin et al. 1993; Dong et al. 2014; Montagud-Camps et al. 2018).

We start with the MHD equations for the density ρ, (isotropic) pressure P, velocity fluctuation $u = U - U_0 \hat{e}_r$ (where U is the total velocity and U_0 is the mean radial flow amplitude), and magnetic field B. Consider a Cartesian frame with XYZ coordinates, the X-axis parallel to the radial passing through

the middle of the box, and change to a Galilean frame moving with the mean wind along the radial coordinate. In this frame, the plasma volume is uniformly stretched in the transverse directions (see Figure 1(b)), thus neglecting curvature terms.

All fields are assumed periodic in the comobile coordinates x, y, and z:

$$t = \tau, \tag{1}$$
$$x = (X - U_0 \tau)/a_x, \tag{2}$$
$$y = Y/a(t), \tag{3}$$
$$z = Z/a(t). \tag{4}$$

The parameter

$$a_x = L_x \big/ L_y^0 = L_x \big/ L_z^0 \tag{5}$$

is the initial aspect ratio of the domain (L_x, L_y, and L_z being the size of the domain in the three directions and the suffix "0" denoting the initial value). Note that the radial size L_x is a constant, while the other sizes of the domain increase linearly with time. The parameter $a(t)$ measures the transverse expansion. It is defined as the heliospheric distance $R(t)$ of the barycenter of the plasma domain, normalized by the initial distance R_0:

$$a = R(t) \big/ R_0 = 1 + \epsilon t = L_y \big/ L_y^0 = L_z \big/ L_z^0. \tag{6}$$

In this equation, $\epsilon = da/dt$ is the *expansion parameter*, defined as the initial ratio between the characteristic expansion and turnover times in the transverse directions (perpendicular to the radial),

$$\epsilon = \frac{\tau_{\mathrm{NL}}}{\tau_{\exp}} = \frac{U_0/R_0}{k_y^{00} u_{\mathrm{rms}}^0}, \tag{7}$$

where $k_y^{00} = 2\pi \big/ L_y^0 = 2\pi \big/ L_z^0$ is the initial minimum wavenumber in the transverse directions, and u_{rms}^0 is the initial rms value of the velocity fluctuations. The EBM equations finally read, with dissipation terms omitted,

$$\partial_t \rho + \nabla(\rho u) = -2\rho(\epsilon/a), \tag{8}$$
$$\partial_t P + (u.\nabla)P + \gamma P \nabla.u = -2\gamma P(\epsilon/a), \tag{9}$$
$$\partial_t u + (u.\nabla)u + \nabla(P + B^2/2)/\rho - B.\nabla B/\rho = -\vec{\mathbb{U}}(\epsilon/a), \tag{10}$$
$$\partial_t B + u.\nabla B - B.\nabla u + B\nabla.u = -\vec{\mathbb{B}}(\epsilon/a), \tag{11}$$
$$P = \rho T, \tag{12}$$

where $\mathbb{U} = (0, u_y, u_z)$ and $\mathbb{B} = (2B_x, B_y, B_z)$. The nabla operator that appears in the previous equations is written in terms of comobile coordinates as $\nabla = (1/(a_x)\partial_x, (1/a(t))\partial_y, (1/a(t))\partial_z)$. The plasma is transported radially, which implies that, in a local Cartesian coordinate system (x, y, z), where x

Table 1
Initial Conditions for the Simulations

Run	ϵ	m^0	Δk	σ_c^0	$\boldsymbol{B}_{t=0}^0$	a_x	$\mu_0[10^{-4}]$
hA0, 5, 8	0	$-5/3$	16	0, 0.5, 0.8	[1, 0, 0]	1	2
hB0, 5, 8	0	-1	16	0, 0.5, 0.8	[1, 0, 0]	1	2
eA0, 5, 8	0.4	$-5/3$	64	0, 0.5, 0.83	[2, 0.4, 0]	5	1.3
eB0, 5, 8	0.4	-1	64	0, 0.5, 0.83	[2, 0.4, 0]	5	1.3
eC5, 8	0.4	$-3/2$	64	0.5, 0.83	[2, 0.4, 0]	5	1.3
eE8	0.4	-1.25	64	0.83	[2, 0.4, 0]	5	1.3
hA8k4	0	$-5/3$	4	0.8	[1, 0, 0]	1	1
eA8k16	0.4	$-5/3$	16	0.83	[2, 0.4, 0]	5	1.3
eC8a1	0.4	$-3/2$	64	0.83	[2, 0.4, 0]	1	1.3
eC8a3	0.4	$-3/2$	64	0.83	[2, 0.4, 0]	3	1.3
hA8b5	0	$-5/3$	16	0.8	[5, 0, 0]	5	2
eC8b6	0.4	$-3/2$	64	0.83	[6, 1.2, 0]	5	1.3
e2A0, 5, 8	0.2	$-5/3$	64	0, 0.5, 0.83	[2, 0.4, 0]	5	1.3
e2B0, 5, 8	0.2	-1	64	0, 0.5, 0.83	[2, 0.4, 0]	5	1.3

Note. From left to right: name of the run, expansion parameter ϵ, initial spectral index m^0, initial power-law extent Δk, normalized cross helicity σ_c^0, initial mean magnetic field vector $\boldsymbol{B}_{t=0}^0$, aspect ratio of the numerical domain a_x, and dynamic viscosity μ_0. Note that the first four rows group together runs with three different values of cross helicities. Resolution is 512^3 for all runs. All runs are integrated during 10 nonlinear times, except run e$B8$, which ends at $t = 20$.

represents the local radial direction, it expands in directions y and z perpendicular to the local radial direction (Figure 1(b)).

Expansion modifies the evolution in two ways: (i) by damping the different fields' amplitudes (see the right-hand side terms in Equations (8)–(12)) and (ii) by damping the gradients perpendicular to the radial due to the $1/a(t)$ factor in the nabla expression. Explicit viscoresistive terms (not shown) are added to the previous equations in order to dissipate the energy that is transported along the spectrum down to the smallest available scales. This energy is given to the internal energy. Note that in the expanding case, the viscoresistive terms are modified in order to minimize the decrease of the Reynolds number with time (Montagud-Camps et al. 2018).

Note that if we choose $\epsilon = 0$ in Equations (8)–(12), we recover the standard compressible MHD equations.

Finally, we define the so-called Elsässer variables,

$$z_\pm = u \mp \text{sign}(B_x^0)\delta B \big/ \sqrt{\rho}, \quad (13)$$

where $\delta B = B - B^0$. We define the normalized cross helicity (hereafter simply called "cross helicity") as the relative energy excess in the z_+ mode:

$$\sigma_c = \frac{E_+ - E_-}{E_+ + E_-} = \frac{\langle z_+^2 \rangle - \langle z_-^2 \rangle}{\langle z_+^2 \rangle + \langle z_-^2 \rangle}. \quad (14)$$

2.2. Numerics, Initial Conditions

Periodic boundary conditions are assumed in all directions of a cube of side 2π in the comobile variables x, y, and z. We use a standard pseudospectral code to numerically solve the above 3D EBM equations with a guide field. All results are from runs with a resolution of $N^3 = 512^3$ grid points. A third-order Runge–Kutta time integration scheme is used.

The initial state consists of nonzero amplitudes for the $z_+(k)$ and $z_-(k)$ fields, excited within shells $1 \leqslant k \leqslant \Delta k$, with $k = |k|$ (in units of $2\pi L_y/l$, with l the wavelength), and weighted so that the 1D spectral index is approximately m^0. Initial incompressibility is obtained by imposing $\boldsymbol{k}.z_\pm(\boldsymbol{k}) = 0$. Density and pressure are uniform. The velocity fields and magnetic fluctuations are then deduced from the $z_\pm$ fields using the definition

(Equation (13)). Random phases are chosen for both z_+ and z_- fields, which implies that $z_+(k)$ and $z_-(k)$ are uncorrelated, thus leading (since $\langle z_+.z_- \rangle = u^2 - b^2/\rho$) to $u_{\text{rms}} \simeq b_{\text{rms}}/\sqrt{\rho}$. Amplitudes are chosen so as to lead to the chosen initial cross helicity σ_c^0.

Figure 1 shows in a schematic way the evolution of the plasma volume from start to end (after 10 nonlinear times) in the two kinds of simulations: (a) homogeneous and (b) expanding. In the latter case, the plasma volume is transported from the initial heliocentric distance R_0 to $5R_0$, with $R_0 = 0.2$ au.

In the homogeneous case (a), the mean magnetic field is parallel to the x axis and remains so. The aspect ratio of the domain is adapted to the amplitude of the mean field so that $B_0/L_x = b_{\text{rms}}/L_y = b_{\text{rms}}/L_z$.

In the expanding case (b), we do not start with a mean field aligned with the radial, as this is not the standard situation. Instead, we adopt a slightly rotated configuration ($B_y^0/B_x^0 = 0.2$). In this way, due to the expansion of the plasma volume in the transverse directions during transport, the conservation of magnetic flux through the expanding faces of the volume leads to $B_y^0/B_x^0 = 1$; i.e., the mean field progressively rotates to an angle of 45^0 with respect to the radial, a standard value at 1 au. The initial domain (as well as the initial eddies) is chosen in most of our simulations to be elongated in the radial direction (i.e., with an aspect ratio $a_x = 5$), so that at the end, the domain aspect ratio is unity. The interest of this choice is rationalized in Section 4.2.

Table 1 presents the list of runs considered here. Parameters are the expansion parameter ϵ (Equation (7)); the initial spectral index m^0, which is imposed in a wavenumber interval Δk starting from the minimum wavenumber; the initial value of the normalized cross helicity σ_c, defined as the relative excess of dominant energy; the initial aspect ratio of the domain $a_x = L_x/L_y = L_x/L_z$; the mean magnetic field $\boldsymbol{B}_{t=0}^0$; and the dynamic viscosity μ_0.

As already mentioned, the initial turbulent Mach number is $M = u_{\text{rms}}/c = 0.12$, with $c = ((5/3)(P/\rho))^{1/2}$, where P is the gas pressure and ρ is the density. Such a low Mach number implies quasi-incompressibility, which allows one to consider the two Elsässer energies as quasi-inviscid invariants, i.e., leading to separate cascades of the two energies. Most runs

have $\epsilon = 0.4$, which corresponds to about a 1 day timescale in Helios data at 1 au, at solar minimum, while the value $\epsilon = 0.2$ corresponds to an 8 hr scale (Montagud-Camps et al. 2020). With one exception, the value of the initial spectral slope m^0 is -1, $-5/3$, or $-3/2$; as we will see, this leads to nonnegligible differences in the evolution of the spectra. The effect of varying the spectral extent Δk, aspect ratio a_x (Equation (5)), and mean magnetic field will be discussed in detail in Section 4.

2.3. Diagnostic Tools, Initial Spectra

Simulations provide 3D energy spectra E^{3D}, from which we deduce 1D energy spectra in the three xyz directions,

$$E(k_x) = \int E^{3D}(k_x, k_y, k_z) dk_y dk_z, \qquad (15)$$

and similarly for the other two spectra, $E(k_y)$ and $E(k_z)$. The 1D spectra will show either total energy (E_T), that is, kinetic + magnetic energy per unit mass, or, most of the time, the E_+ and E_- spectra separately. In the expanding case, the $0x$ direction is that of the radial, with the plane $x0y$ containing the mean magnetic field direction.

In the following, we use either physical or normalized wavenumbers. For physical wavenumbers (k_x, k_y, or k_z), we use as a unit wavenumber the initial smallest transverse wavenumber,

$$k_y^{00} = 2\pi/L_y^0, \qquad (16)$$

where L_y^0 is the transverse size of the initial numerical domain. Due to differences in both initial conditions and anisotropy evolution, it will also prove useful to use normalized wavenumbers when comparing spectra with and without expansion. This simply consists of normalizing the abscissa (either k_x, k_y, or k_z) by its minimum value when plotting spectra.

Spectral indices will be defined as

$$m_\pm = \log(E(k_i = k_2)/E(k_i = k_1))/\log(k_2/k_1), \qquad (17)$$

where k_i can be either k_x, k_z, or an equivalent of k_z, for which one takes the average of the two spectra $E(k_y)$ and $E(k_z)$. Note that the interval $[k_1, k_2]$ will be fixed in normalized coordinates. We present in Figure 2 the initial total energy spectra versus physical wavenumbers k_x (solid line), k_y (dotted), and k_z (dashed) for the four series of runs hAs, hBs, eAs, and eBs. All spectra are compensated by $k^{-5/3}$. One sees that for homogeneous runs hAs and hBs, the 1D spectra occupy the same wavenumber range in all three directions; this corresponds to the domain aspect ratio $a_x = 1$. For runs with expansion, the radial ($E(k_x)$) spectrum is shifted with respect to the two spectra $E(k_y)$ and $E(k_z)$, which corresponds to the domain aspect ratio $a_x = 5$.

As seen in the figure, another difference between the homogeneous and expanding simulations is the initial extent of the excited spectrum, which is $\Delta k = 16$ in the homogeneous runs and $\Delta k = 64$ in the expanding runs (see Table 1). It is seen that in the figure, the scaling is constant only in the first half of the interval Δk, while the spectrum is becoming steeper in the second half of the interval. Also, even in the first half of the excited interval, the spectra are actually somewhat steeper than the imposed scaling k^{m^0}, as is clearly seen from the two cases with $m^0 = -5/3$. The value m^0 is thus to be taken as a plain
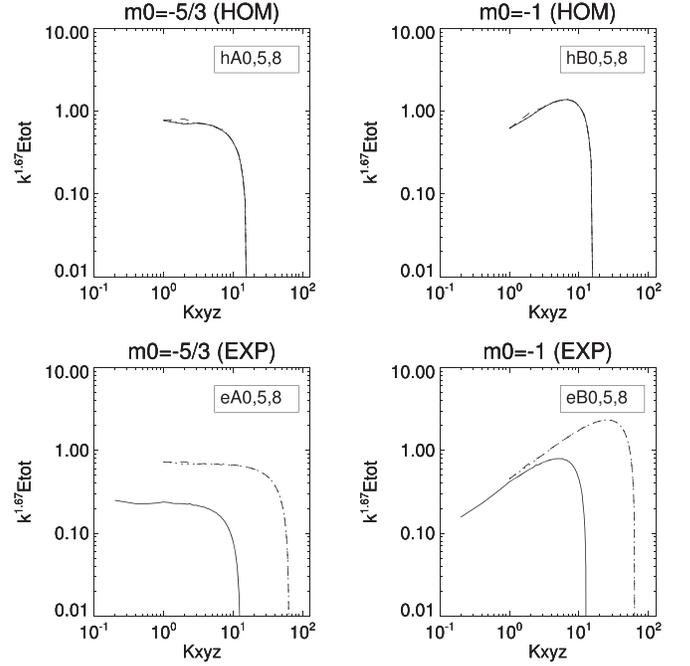

Figure 2. Initial 1D total energy spectra for runs hAs, hBs, eAs, and eBs. Each panel shows the 1D spectra in the three directions: $E_T(k_x)$ (solid), $E_T(k_y)$ (dotted), and $E_T(k_z)$ (dashed). All spectra are compensated by $k^{-5/3}$. As a rule, $E_T(k_y)$ and $E_T(k_z)$ are almost indistinguishable.

indication, while meaningful evaluations of the spectral indices $m_\pm$ (see Equation (17)) will be given when analyzing the time evolution of the spectra in the next section.

3. Results

3.1. Varying σ_c^0 and m^0

We first consider the effect of varying the initial cross helicity σ_c^0 and spectral index m^0.

3.1.1. Global Quantities

Here we consider global quantities versus time: the two Elsässer energies $E_\pm = \langle z_\pm^2/2 \rangle$, the ratio $b_{rms}/|B^0|$, and the normalized cross helicity $\sigma_c(t)$.

Figure 3 shows the decay of the dominant and subdominant energies E_+ and E_- versus time. Results for the homogeneous ($hA_{0,5,8}$) and expanding ($eA_{0,5,8}$) runs are given in the left and right panels, respectively. In each panel, solid, dotted, and dashed lines indicate, respectively, $\sigma_c^0 = 0$, 0.5, and 0.8 (for homogeneous runs) or 0.83 (in the expanding case). As expected, when σ_c^0 is nonzero, cross helicity is seen to grow with time for homogeneous runs and decay for expanding runs. We consider in Figure 4 the decay of energies $E_\pm$ versus radial distance R in the expanding case; in the left panel, we show the three runs $eA_{0,5,8}$ with $m^0 = -5/3$, and in the right panel, we show the three runs $eB_{0,5,8}$ with $m_0 = -1$. The $1/R$ WKB energy decay appears as a short thin solid line. The two long thin solid lines correspond to the mean $E_\pm$ energy decay found by Bavassano et al. (2000, 2002) in Helios data. Run $eB8$ is closer to these observations than run $eA8$; clearly, the energy decay curves for both E_+ and E_- depend on the initial conditions.

Figure 5 shows $b_{rms}/|B^0|$ and σ_c versus time stacked on one another for runs hAs, hBs, eAs, and eBs, i.e., varying σ_c^0 and m^0.
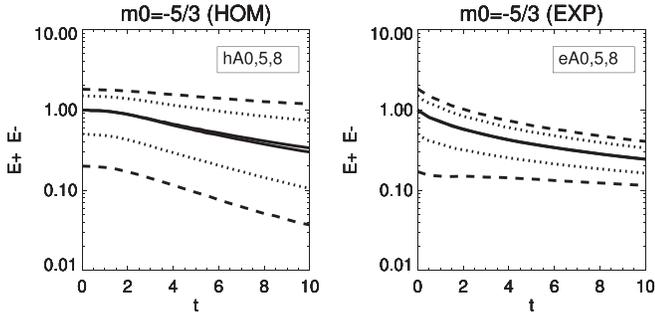
Figure 3. Varying cross helicity: total energies $E_\pm$ vs. time for homogeneous runs *hAs* and runs with expansion *eAs*. Here $\sigma_c^0 = 0$, 0.5, and 0.8 (0.83 for the run with expansion) are shown by solid, dotted, and dashed lines, respectively.
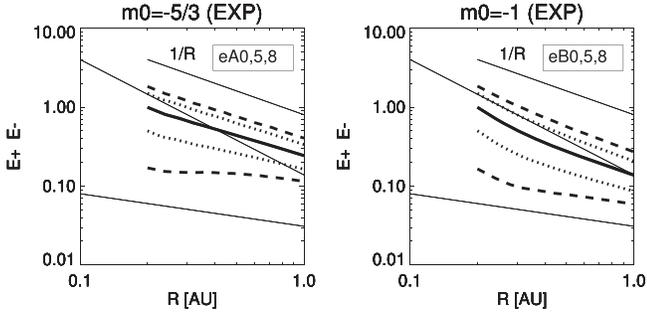

Figure 4. Varying cross helicity: total energies $E_\pm$ vs. heliocentric distance R for runs with expansion *eAs* and *eBs*. Styles are the same as in Figure 3. The two long thin solid lines are the mean energies E_+ and E_- as found by Bavassano et al. (2000, 2002) from Helios data, and the short thin solid line is the $1/R$ (WKB) decay.

In each case, $\sigma_c^0 = 0$, 0.5, and 0.8 (or 0.83 in the expanding case) are shown, respectively, with solid, dotted, and dashed lines. For the homogeneous runs (top panels), the mean magnetic field is constant; thus, as expected, $b_{\rm rms}/|B^0|$ is decaying with time. Also, increasing σ_c^0 leads to slower magnetic energy decay. This is not so surprising, since an increase in σ_c^0 leads to a smaller z_- and thus a longer turnover time for z_+ (and thus for $b_{\rm rms}$: $\tau_{\rm NL}^+ = 1/(kz_-)$. On the contrary, runs with expansion (bottom panels) show increasing $b_{\rm rms}/|B^0|$ because expansion more strongly damps the radial component of the mean field than fluctuations due to the linear Alfvén coupling.

Note that, for the expanding case, the three curves do not depend much on cross helicity. This means that the main source of damping is expansion, not turbulent decay, as could be suspected by remarking that the decay of the dominant energy curve in Figure 4 is not very different from the WKB $1/R$ law. Note also that the time evolution of $b_{\rm rms}/B_0$ depends strongly on the initial angle of the mean magnetic field with the radial; it is clear that starting with a large angle will lead to a much slower decrease of B_0, while the contrary will occur if the initial angle is close to zero. The angle we considered here has been chosen to match the average observed angle at 1 au, i.e., 45^0.

Consider now cross helicity versus time. When starting with a nonzero σ_c^0, homogeneous flows (top panels) show a clear increase of σ_c due to the larger relative decay rate of the minor species z_-. This is explained by the fact that the minor species cascade is driven by the dominant amplitude, thus leading to a rapid decay of the minor species, called "dynamic alignment" (Dobrowolny et al. 1980; Matthaeus & Montgomery 1980; Grappin et al. 1982). On the contrary, flows with expansion
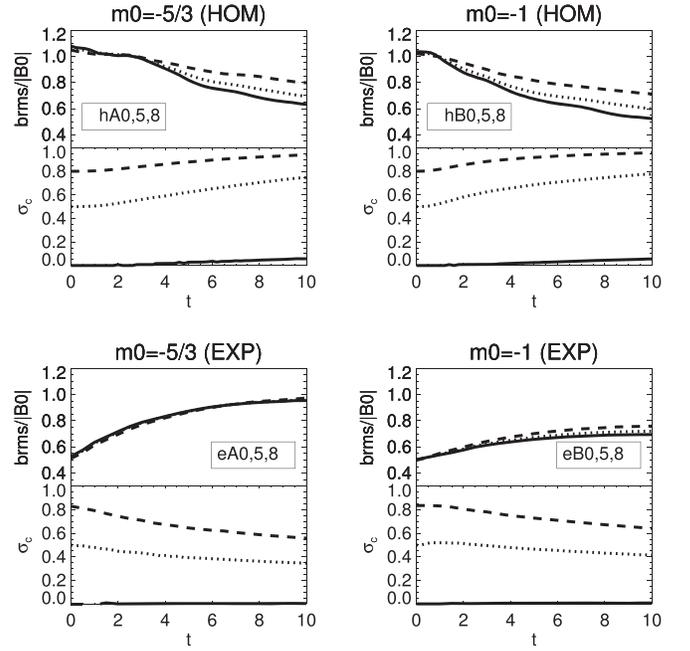

Figure 5. Varying cross helicity and initial spectral index $b_{\rm rms}/B_0$ (top) and cross helicity σ_c vs. time. Styles are the same as in Figure 3.

(bottom panels) show a decrease of σ_c with time (and thus distance). Such a cross-helicity decrease was first observed in Helios and Voyager observations by Roberts et al. (1987). At last, we note (and discuss later below) that the cross-helicity decrease is slower when starting with flatter spectra (compare the two bottom panels, runs *eA*5,8 and *eB*5,8).

3.1.2. Spectral Quantities

We present in Figure 6 a cut at $k_z = 0$ of the 3D E_+ spectra at times zero and 10 for the two runs with initial large cross helicity, with the homogeneous in the top panels (*hA*8) and expansion in the bottom panels (*eA*8). The direction of the mean magnetic field is indicated by a straight line, which in the expanding case rotates progressively so that it is 45^0 off the radial at the end of run *eA*8. We see that the direction of the cascade is perpendicular to B_0 in both runs, and that it rotates with B_0 in the expanding case. Note that other anisotropies are possible in the expanding case; starting with a quasi-isotropic spectrum and a large enough expanding rate generally leads to spectra aligned with the radial direction, a source of the second branch in the so-called Maltese cross (Matthaeus et al. 1990; Verdini & Grappin 2016; Montagud-Camps et al. 2020).

We next consider in Figure 7 the 1D reduced spectra $E_\pm(k)$ averaged during the interval $8 \leqslant t \leqslant 10$ for the four families of runs *hA*0, 5, 8; *hB*0, 5, 8; *eA*0, 5, 8; and *eB*0, 5, 8. The spectra $E_+(k)$ and $E_-(k)$ are compensated by $k^{-3/2}$. Ordinates are arbitrary, chosen to optimize readability. Recall that different directions are used for the homogeneous and expanding runs. For the homogeneous runs, we plot the average of the spectra $E(k_y)$ and $E(k_z)$, i.e, spectra in directions perpendicular to the mean magnetic field, while for the runs with expansion, we plot $E(k_x)$, that is, in the radial direction. In both cases, we normalize the wavenumbers by their minimum values.

We added vertical dotted lines at $k = 4$ and 10, which we will consider from now on as markers of the inertial range
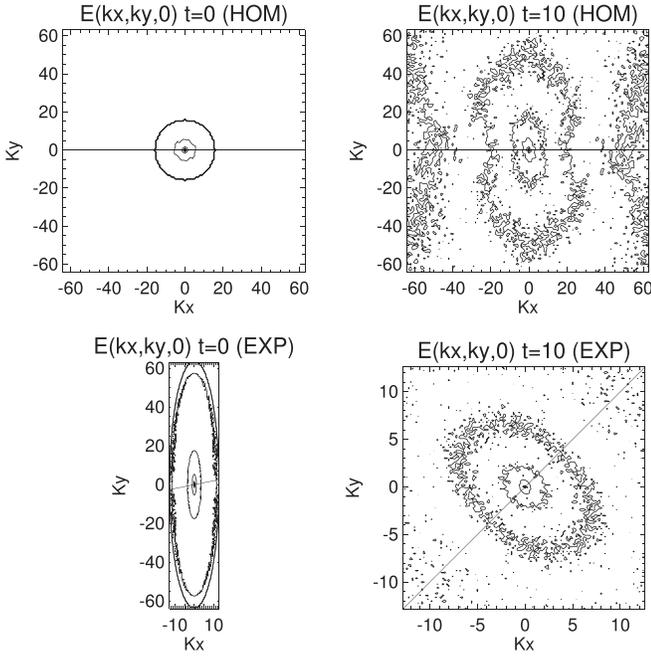
Figure 6. Cuts at $k_z = 0$ of 3D $E_+(k_x, k_y, k_z = 0)$ spectra at time $t = 0$ and 10. Straight lines indicate the direction of the mean magnetic field. Top panels: homogeneous run $hA8$. Bottom panels: run with expansion $eA8$. The unit wavenumber is $2\pi/L_y^0$, where L_y^0 is the initial transverse size of the domain.
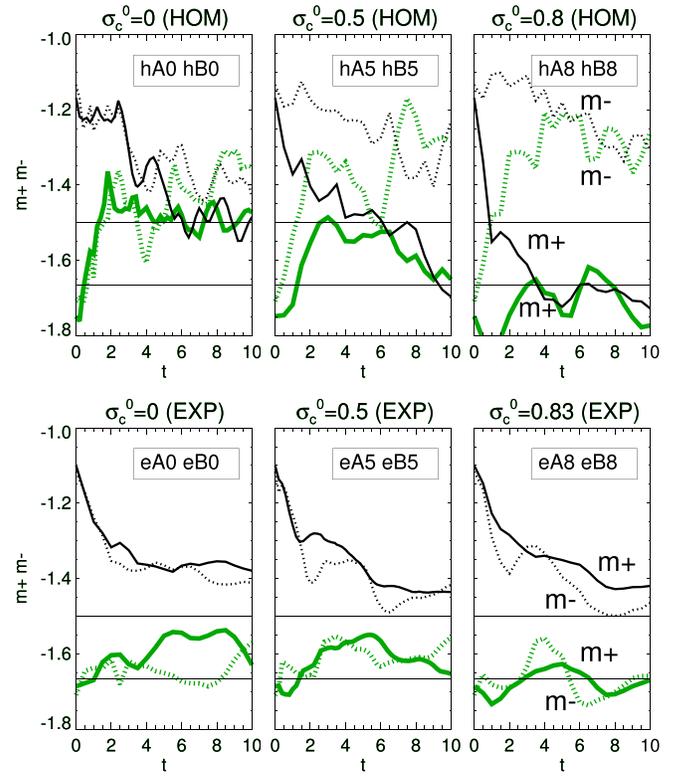

Figure 7. Varying σ_c^0 and m_0. Shown are the 1D reduced energy spectra $E_+(k)$ and $E_-(k)$ in normalized coordinates, compensated by $k^{-3/2}$ and averaged in the time interval $8 \leqslant t \leqslant 10$. The ordinates are arbitrary to maximize readability. The runs are hAs, hBs, eAs, and eBs. Styles are the same as in Figure 3. Vertical dotted lines ($k = 4$ and 10 in normalized coordinates) indicate the wavenumber interval chosen to compute spectral indices in the following.

Figure 8. Varying σ_c^0 and m_0. Shown are indices m_+ and m_- vs. time (solid and dotted lines, respectively) computed in the normalized wavenumber interval $4 \leqslant k \leqslant 10$. Each panel shows two runs with a given σ_c^0 (from left to right, 0, 0.5, 0.8, 0, 0.5, and 0.83). Runs with $m_0 = -5/3$ appear as double thick green lines, and runs with $m_0 = -1$ appear as thick black lines. Solid horizontal lines mark spectral indices $-3/2$ and $-5/3$.
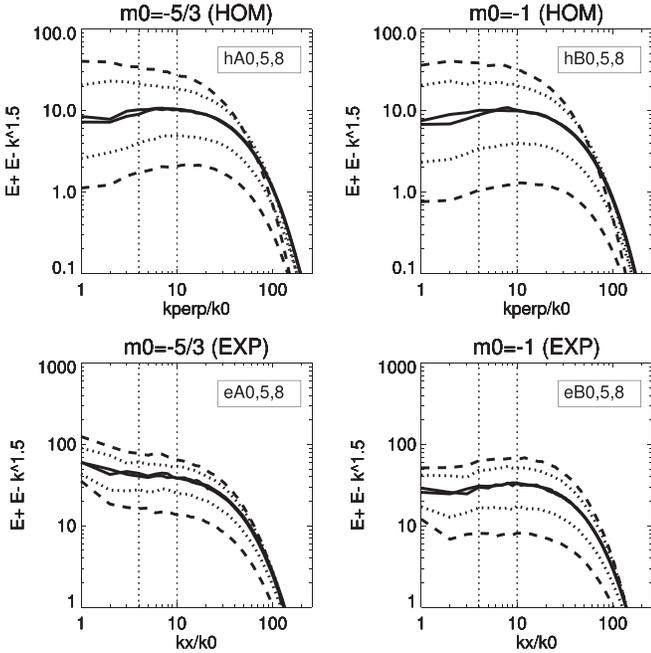
the dependence (or not) on initial conditions. First, in runs with nonzero σ_c^0, cross helicity is concentrated on the largest scales in the homogeneous runs, while in the expanding runs, it is either uniformly distributed or showing a minimum at the largest scale. Second, in the homogeneous runs, the final slope does not depend on the initial slope, while in the runs with expansion, it does.

These properties are well visible in Figure 8, where we show the evolution of the two spectral indices m_+ and m_- with time, computed in the interval $4 \leqslant k \leqslant 10$. Cross helicity grows from left to right, with the homogeneous runs appearing in the top panels and runs with expansion in the bottom panels. Each panel allows one to compare the evolution of indices m_+ (solid lines) and m_- (dotted lines) with two different starting indices: $m_0 = -5/3$ in double thick green lines and -1 in thick black lines.

Homogeneous and expanding runs show completely different evolutions. Expanding runs are almost independent of cross helicity and show simple properties: (i) the two indices converge toward values that depend strongly on their initial values, and (ii) the two indices m_+ and m_- remain about equal. For homogeneous runs, we see that (i) m_+ and m_- converge toward values that do not depend on their initial value, and (ii) when cross helicity is substantial, indices become unequal, with $|m_+| > |m_-|$; i.e., E_+ becomes steeper than E_-. This behavior was first found in closure calculations by Grappin et al. (1983) and commonly denoted as "spectral pinning" (Lithwick & Goldreich 2003), as discussed below.
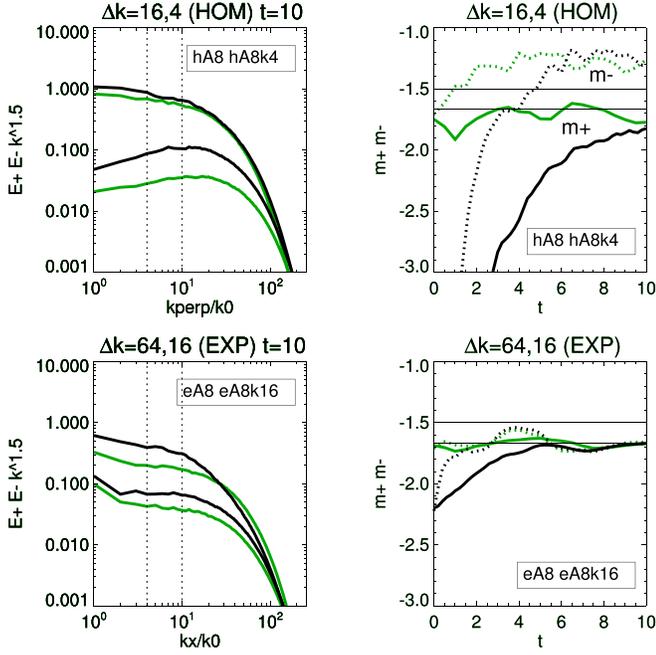
boundaries, since spectra can be approximated by power laws in this range.

Examining the different spectra shows interesting differences in the distribution of cross helicity along the spectral range and

Figure 9. Varying the initial spectral extent Δk: $E_\pm$ spectra compensated by $k^{3/2}$ at $t = 10$ (left panels) and spectral indices (right panels). Top panels: homogeneous runs $hA4$ (green lines) and $hA8k4$ (with reduced Δk; black lines). Bottom panels: expanding runs $eA8$ (green lines) and $eA8k16$ (with reduced Δk; black lines). Spectra are compensated by $k^{-3/2}$, with vertical dotted lines marking the inertial range. Solid and dotted lines show the m_+ and m_- indices, respectively.

Figure 10. Increasing the initial mean magnetic field $\boldsymbol{B}_0$: spectral indices m_+ (solid lines) and m_- (dotted lines) vs. time. Starting at the top left panel, we show (i) homogeneous runs $hA8$ with $\boldsymbol{B}_0 = (1, 0, 0)$, (ii) $hA8b5$ with $\boldsymbol{B}_0 = (5, 0, 0)$, (iii) runs with expansion $eC8$ with $\boldsymbol{B}_0 = (2, 0.4, 0)$, and (iv) $eC8b6$ with $\boldsymbol{B}_0 = (6, 1.2, 0)$. Homogeneous runs have $\sigma_c^0 = 0.8$, and runs with expansion have $\sigma_c^0 = 0.83$.

3.2. Spectral Extent Δk, Mean Magnetic Field, and Expansion Parameter ϵ

In series hAs, hBs, eAs, and eBs analyzed above, we varied σ_c^0 and m_0. A look at these runs in Table 1 also shows that a_x, Δk, and B_0 are systematically different in the homogeneous and expanding runs. We thus consider here the successive effect of varying Δk, $\boldsymbol{B}_{t=0}^0$, as well as an intermediate value of the expansion parameter ϵ between 0 and 0.4. We postpone the case of the initial aspect ratio of the domain a_x to the Section 4.

In Figure 9, we consider two runs, one homogeneous ($hA8$) and one with expansion ($eA8$) with high cross helicity and $m^0 = -5/3$. Each one is compared with a similar run with Δk four times smaller ($hA8k4$ and $eA8k16$). The left panels show the spectra at time $t = 10$, and the right panels show the spectral indices $m_\pm$ versus time. Homogeneous runs are shown in the top panels, expanding runs in the bottom panels. Runs with large Δk appear in green lines, and runs with reduced Δk appear in black lines.

Decreasing Δk produces initially steeper spectra, as seen in the right panels (black lines), for both the homogeneous and expanding runs. This is due to the initial lack of excitation in the reference interval [4, 10]. However, at $t = 10$, the final slopes become comparable to those of runs with the standard values of Δk, as seen in the right panels. We conclude that the choice of different values of Δk (16 and 64) for the homogeneous and expanding runs are of minor importance, as relaxation toward the same turbulent state is ensured whatever the value of Δk, albeit more or less rapidly.

In Figure 10, we show the effect of increasing the initial mean magnetic field from $\boldsymbol{B}^0 = (1, 0, 0)$ to $(5, 0, 0)$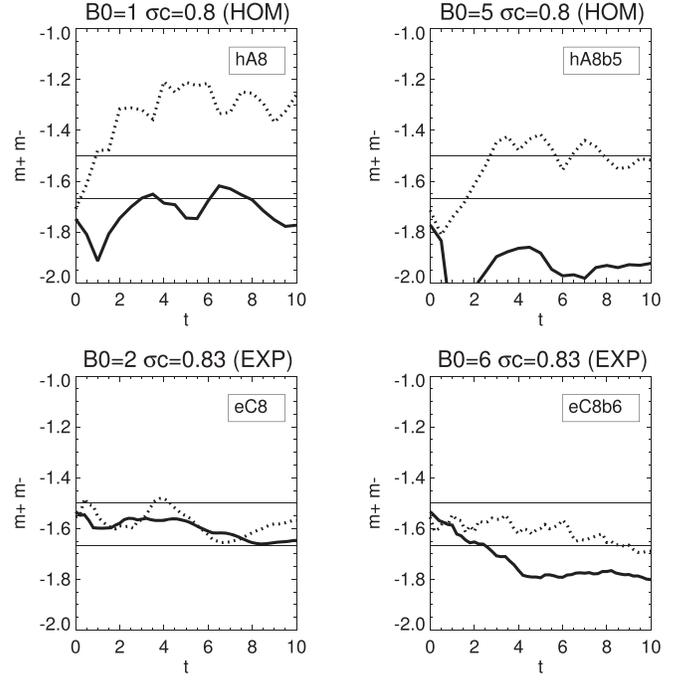 in the homogeneous case (runs $hA8$ and $hA8b5$) and from $\boldsymbol{B}^0 = (2,$ 0.4, 0) to (6, 1.2, 0) in the expanding case (runs $eC8$ and $eC8b6$; see Table 1).

In both the homogeneous and expanding cases, it is seen that increasing the mean magnetic field leads to steeper spectra. The effect is stronger in the homogeneous case. Such an effect has been observed in several works investigating the transition from strong to weak anisotropic cascade, albeit with zero cross helicity (Dmitruk et al. 2003; Rappazzo et al. 2007; Perez & Boldyrev 2008). Note also that the spectral pinning (i.e., $|m_+| > |m_-|$) we have observed previously in homogeneous runs is seen to appear here in expanding runs, as well when the mean field is large enough.

We finally show in Figure 11 the indices $m_\pm (t)$ with half our standard value of the expansion rate, i.e., $\epsilon = 0.2$. We consider the usual three values of cross helicity, 0, 0.5, and 0.83, and the two starting indices $m_0 = -5/3$ (green lines) and -1 (black lines). The resulting curves are globally similar to those shown in the bottom panels of Figure 8; however, one sees for runs with nonzero σ_c^0 and $m^0 = -5/3$ the appearance of some pinning ($|m_+| > |m_-|$), albeit more moderate than previously seen in homogeneous runs (top panels in Figure 8).

4. Discussion

We have compared in this paper the results obtained on the turbulent evolution using two models: (i) homogeneous MHD and (ii) MHD with expansion. We first summarize the properties predicted by the two models, and then we discuss the validity of the parameters chosen.
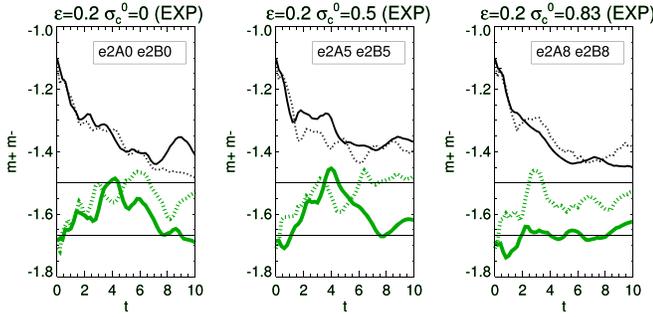
Figure 11. Intermediate expansion rate $\epsilon = 0.2$. Shown is the time evolution of indices m_+ and m_-, computed in $4 \leqslant k/k_0 \leqslant 10$ for six runs, with growing initial cross helicity from left to right. See Figure 8 for styles. Green lines denote runs with $m^0 = -5/3$, and black lines are runs with $m^0 = -1$.

Figure 12. Varying the domain aspect ratio a_x in expanding runs $eC8a1$, $eC8a3$, and $eC8$. Shown are the 1D spectra at $t = 10$ in different directions using physical wavenumbers $E_\pm(k_x)$ (solid lines) and $E_\pm(k_y)$ (dotted lines). From left to right, $a_x = 1$, 3, and 5. The two vertical dotted lines mark the boundaries of the inertial range adopted above; see text. The unit length is $L_y^0/(2\pi)$.

4.1. Contrasted Properties of the Two Models

In homogeneous MHD simulations, spectral pinning is found, that is, a steeper dominant component E_+, with the difference between the two indices m_+ and m_- increasing when cross helicity is larger. In other words, the spectral indices depend on total cross helicity. This is not compatible with the usual picture proposed by the strong perpendicular cascade (that is, perpendicular to the mean magnetic field), for which both spectra E_+ and E_- are parallel, with $m_+ = m_- = -5/3$ (Lithwick et al. 2007); instead, it is compatible with the weak isotropic cascade prediction of the generalized Iroshnikov–Kraichnan theory (Grappin et al. 1983), for which $m_+ + m_- = -3$. This value is found in our homogeneous runs when the mean magnetic field is not too much larger than unity. The pinning phenomenon has been found in previous MHD simulations. First, in 2D incompressible MHD simulations (with no mean field), the weak isotropic version is found ($m_+ + m_- = -3$) in Pouquet et al. (1988). More recently, Perez & Boldyrev (2010) found it but, to explain why solar wind observations show no spectral pinning, proposed that the solar wind turbulence are forced to exhibit parallel $E_\pm$ spectra due to a quasi-infinite inertial range resulting from an infinite Reynolds number.

We have seen that spectral pinning is absent from our simulations with expansion as soon as the expansion parameter is large enough and the mean magnetic field is not much larger than the $b_{\rm rms}$ amplitude. In that case, the two spectra $E_\pm$ are indeed more or less parallel, i.e., $m_+ \simeq m_-$, as observed in solar wind spectra (Grappin et al. 1990; Chen et al. 2020). As a rule, initially steep spectra (e.g., $m_0 \simeq -5/3$) remain steep at larger distances, while initially flat spectra (e.g., $m \simeq -1$) steepen and relax to intermediate index values, e.g., -1.5. Again, a similar behavior is observed in solar wind data (Chen et al. 2020). In the homogeneous case, on the contrary, the relaxed spectral index is independent of the initial spectral index, as expected in a turbulent state.

In the rest of the discussion below, we consider in turn the following issues:

(i) the choice of the initial domain aspect ratio for the expanding cases;
(ii) the difference between radial and perpendicular directions in the expanding cases;
(iii) the relation between spectral index and cross correlation;
(iv) the origin of the absence of pinning in the solar wind; and
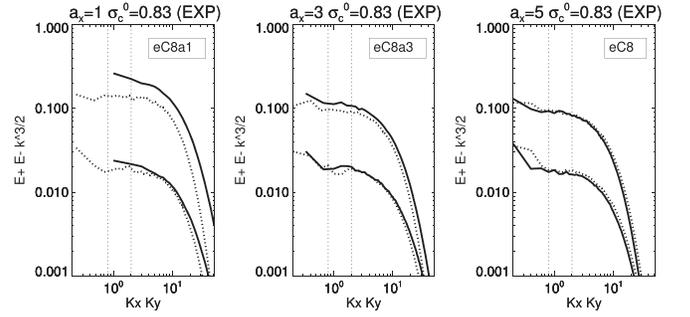(v) the reason that the spectral index does not always converge to $-5/3$ in expanding runs.

4.2. Domain Aspect Ratio

In the simulations with expansion examined up to now, we started with a numerical domain extended in the radial direction by a factor of 5 ($a_x = 5$), thus arriving at the end at a cubic domain. A cubic domain is a priori supposed to favor the local nonlinear interactions, which are necessary to ensure a "normal" turbulent cascade. However, the opposite choice ($a_x = 1$) is also possible; in that case, local interactions are maximum at the beginning of the evolution, not at the end. We compare in Figure 12 the two cases at the end of the simulation, $t = 10$, further adding a run with the intermediate value $a_x = 3$.

The figure shows $E_\pm$ spectra along k_x (solid lines) and k_y (dotted lines) for the runs with expansion (from left to right): $eC8a1$, $eC8a3$, and $eC8$ with $a_x = 1$, 3, and 5, respectively. The inertial range is marked by dotted lines as previously. Note that we use physical wavenumbers, so that the inertial range is given by $4/5 \leqslant k \leqslant 10/5$ (the factor $1/5$ is due to the fact that the final transverse size is five times the initial one in all three runs).

We see that, for both $a_x = 5$ and 3, turbulence at $t = 10$ is quasi-isotropic, which means that the coupling between the radial direction and the perpendicular plane is efficient, while it is much less so when $a_x = 1$, which is probably due to the too-large importance of nonlocal interactions in this case, at least at the end of the computation. From this, we conclude that choosing a_x between 3 and 5 is a reasonable choice. See Montagud-Camps et al. (2020) for a similar discussion in the context of turbulent dissipation with a large turbulent Mach number.

4.3. Radial versus z Direction

In simulations with expansion, we have chosen to measure spectral scaling in the radial direction to allow direct comparison with observations. It is of interest to also examine the scaling in directions perpendicular to the mean field for the sake of comparison with the scaling obtained in homogeneous runs and because the preferred cascade develops perpendicularly to the mean magnetic field (Figure 6).

In Figure 13, we compare the spectral evolution along directions k_x (left panels) and k_z (right panels) at times $t = 0$, 2, ..., 10 in the two expanding runs $eA8$ and $eB8$. The $E_\pm$ spectra are compensated by $k^{-3/2}$.

We see that the interval [4, 10] (in normalized coordinates) is a reasonable candidate for the inertial range in both the k_x and
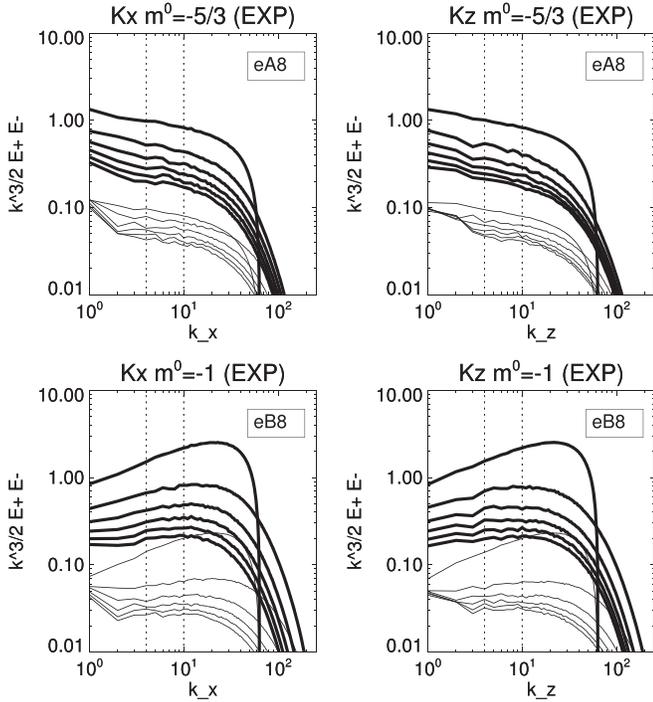
Figure 13. The E_+ (thick lines) and E_- (thin lines) spectra along the radial (k_x; left panels) and perpendicular (k_z; right panels) directions for two runs with expansion: $eA8$ (top) and $eB8$ (bottom). Times $t = 0, 2, ..., 10$, spectra are compensated by $k^{-3/2}$. Dotted lines are the boundaries of the interval used to compute the spectral indices.

k_z directions. Actually, the spectral indices do not seem very different. Figure 14 shows the spectral indices for the two runs separately: left, computed in the k_x direction, and right, in the k_z direction. One sees that in the k_z case, the indices $m_{\pm}$ show larger fluctuations, which is clearly related to the spectra being more irregular. We thus conclude that the differences we have observed up to now in spectral behavior between the homogeneous and expanding runs are not due to our choice of selecting the k_x direction, i.e., not a direction perpendicular to the mean field, in the expanding case.

4.4. Comparison with Helios Data

We attempt here to compare the evolution of some properties of the solar wind turbulence as observed during the Helios 1 mission with those shown by MHD with expansion. A first property is the combined decay of cross helicity with distance and that of the spectral slope. The second is the relation between cross helicity and the spectral index.

The observed turbulent evolution is illustrated in Figure 15 by four averaged spectra E_+ and E_-, compensated by $f^{-5/3}$. The left panel shows fast stream averages ($>500\,\mathrm{km\,s^{-1}}$), and the right panel shows slow stream averages ($<500\,\mathrm{km\,s^{-1}}$). Each panel shows two couples of spectra $E_{\pm}$, one close to the Sun (0.3 au $< R <$ 0.5 au; solid lines) and one far from the Sun (0.8 au $< R <$ 1 au; dotted lines).

Visual inspection shows that (i) cross helicity decreases with distance in either fast or slow streams; (ii) in either fast or slow streams, spectra steepen with distance; (iii) either close to the Sun or (see Chen et al. 2013) close to 1 au, the spectra are flatter when cross helicity is higher; and (iv) the previous property is not built during transport from 0.3 to 1 au but is already present at 0.3 au. Hence, this relation between spectral
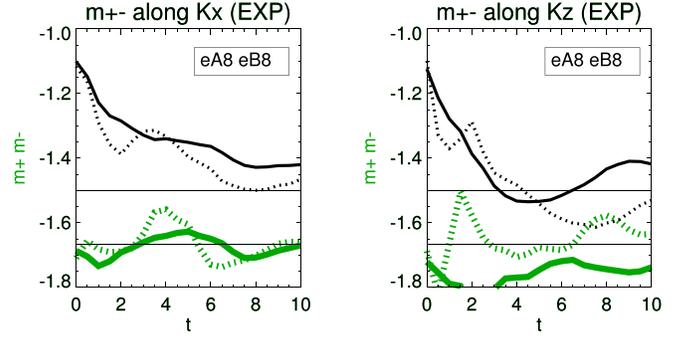

Figure 14. Spectral indices m_+ (solid lines) and m_- (dotted lines) vs. time computed in the radial ($4 \leqslant k_x \leqslant 10$; left panel) and z ($4 \leqslant k_z \leqslant 10$; right panel) directions. Shown are runs $eA8$ (thick green lines) and $eB8$ (thin black lines).
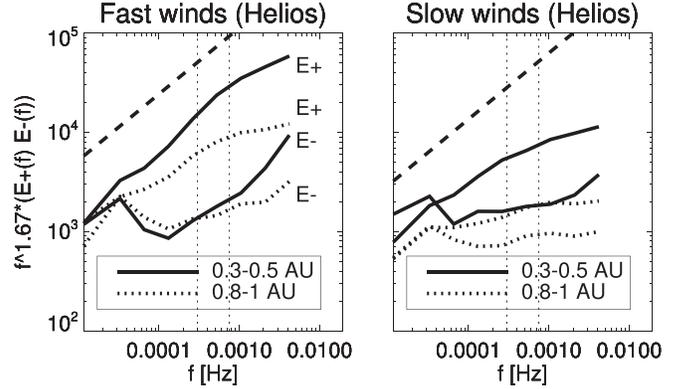

Figure 15. The $E_{\pm}$ spectra of the Helios 1 mission during the first 4 months: relation between spectral index, distance, and cross helicity/wind speed. Fast streams are shown in the left panel, and slow streams are shown in the right panel. Spectra are averaged separately close to the Sun (solid lines) and close to 1 au (dotted lines); see text for details. Vertical dotted lines mark the frequency interval $[f_\star, 2.5f_\star]$ with $f_\star = 3 \times 10^{-4}$ Hz $(1/f_\star \simeq 1$ hr).

index and cross helicity is a by-product of processes acting closer to the Sun, either the low corona or the accelerating region.

We now turn to the simulations with expansion. We show in Figure 16 the index m_+ versus time for two series of runs. In the left panel, we show runs with high cross helicity $\sigma_c^0 = 0.83$, and we show lower cross helicity $\sigma_c^0 = 0.5$ in the right panel. In each case, we vary the initial spectral index m^0 from -1 to $-5/3$. The same style is adopted in the two panels for each pair of runs with the same value of m^0. More precisely, the runs considered for high cross helicity in the left panel are $eB8$, $eE8$, $eC8$, and $cA8$, and those for moderate σ_c^0 in the right panel are $eB5$, $eC5$, and $eA5$.

The insert in each panel shows the evolution of cross helicity with time for the specific runs $eE8$ and $eC5$, denoted respectively in the figures by the letters F and S for "fast" and "slow," to be explained below. Note that the cross-helicity curves shown are representative of the other runs in each of the two panels. So, as we already knew, property (i) is shared with Helios data.

We can also see that $m_+(t)$ is systematically decreasing with time, except when starting from $-5/3$ or close to it. This conclusion might have been guessed already from Figure 8; however, here the larger ensemble of initial indices allows a more secure conclusion. So, property (ii) is also shared by Helios data.
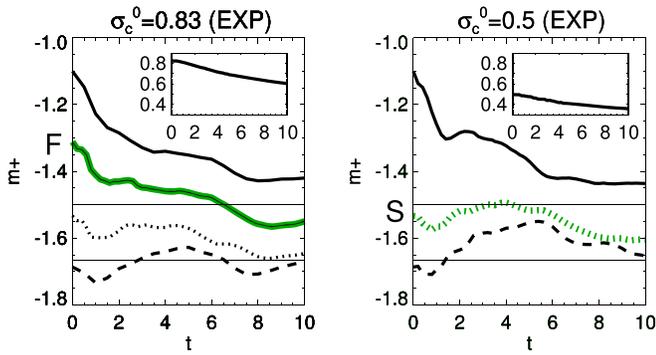
Figure 16. Spectral index m_+ evolution for high and low cross helicity: $\sigma_c^0 = 0.83$ in the left panel and 0.5 in the right panel. In each panel, a series of initial indices m^0 is considered. Inserts show cross-helicity evolution for runs F (left) and S (right).

Note that assuming a wind that would be made with equal weights of all runs shown in the figure would produce no correlation at all between the spectral index and the cross helicity at either $t = 0$ or 10; property (iii) should thus not be recovered. So, let us introduce the correlation at $t = 0$, for instance, by considering the distribution made of just the two runs F and S, defined previously. Run F has a σ_c larger than that of run S, as well as a spectrum flatter than that of run S, at both $t = 0$ and 10 (and in between). As we see in the figure, runs F and S at time $t = 10$ still satisfy the required property. So, property (iii) is probably satisfied, assuming that the solar wind turbulent stream is made of a family of streams with initial properties close to those of runs F and S.

4.5. Why Does Pinning Not Appear in Solar Wind Turbulence?

Figure 17 suggests the solution. It shows in the two left panels the familiar $E_\pm$ spectra at $t = 10$ for the homogeneous run $hA8$ (top) and the expanding run $eA8$ (bottom), both compensated by $k^{-5/3}$. In the two right panels, we plot the magnetic (thick line) and kinetic spectra (thin line). In the expanding run (and not in the homogeneous run), there is a clear magnetic excess at the largest scale. Correspondingly, in the expanding run, one sees that the E_- spectrum also has an "excess" at the largest scale. The interpretation is simple: at the largest scale, the magnetic excess algebraically leads to an excess of E_-. There is thus a permanent large-scale injection of zero cross helicity at the largest scale.

Our final interpretation is that this large-scale injection of a magnetic excess is the source of (i) the decrease with time of the relative cross helicity in the expanding plasma and (ii) the absence of pinning.

Now, how is the magnetic energy excess injected at large scales? A critical scale is the WKB scale, below which magnetic and velocity fluctuations decrease at the same rate with distance $(\delta u = \delta b/\rho^{1/2} \simeq 1/R^{1/2})$. Above this critical WKB scale, expansion dominates; i.e., the Alfvén coupling is inefficient, and the velocity fluctuations damp globally faster than the magnetic fluctuations due to the conservation of magnetic flux, angular momentum, and radial momentum (Zhou & Matthaeus 1990; Grappin et al. 1993; Oughton & Matthaeus 1995; Dong et al. 2014). This is sufficient to generate the magnetic excess as soon as the expansion is large enough for the largest scale of the simulation to indeed be non-WKB. Figures 10 and 11 confirm this, as they show that partial
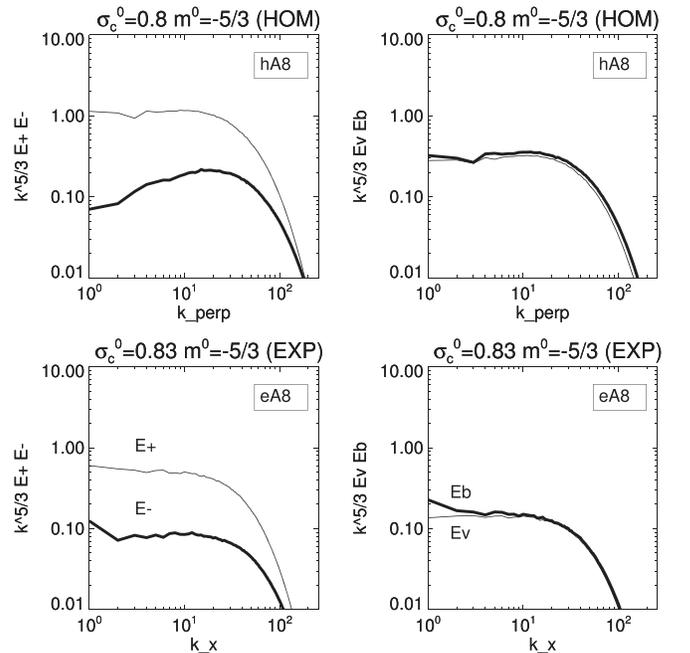

Figure 17. Origin of the suppression of pinning in the expanding case: homogeneous run $hA8$ (top row) and expanding run $eA8$ (bottom). The left panels show $E_\pm$ spectra at $t = 10$, compensated by $k^{-5/3}$. The right panels show Ev (thin lines) and Eb (thick lines) spectra.

pinning reappears when either the expansion parameter is decreased or the mean magnetic field is increased.

On the contrary, whenever the large non-WKB scales gain importance, either because the initial mean magnetic field is decreased or as the expansion rate is increased, one finds (not shown) a large-scale increase of the magnetic excess and an associated acceleration of the normalized cross-helicity decrease.

Note that other large-scale sources of low or zero cross helicity are present in the solar wind, such as shear flows associated with stream structures (Roberts et al. 1991). Stream structures certainly contribute to the decrease of cross helicity with distance, but locally, while the expansion contribution is ubiquitous in the solar wind.

4.6. Why Does the Spectral Index Not Always Converge to −5/3?

When expansion is present, we have seen that the spectral index converges to a value that depends on the initial index m^0, except when the initial slope is close enough to the value $-5/3$. A possible explanation is that, since expansion damps the turbulent amplitude in addition to turbulent dissipation, the nonlinear time is increased; thus, the evolution is slowed down compared to the homogeneous case.

The evolution of the spectral indices $m_\pm$ is shown in Figure 18 up to time $t = 20$ for run $eB8$. One sees that the two indices show no clear drift toward $-5/3$ in the interval $6 \leqslant t \leqslant 20$, remaining at values close to $-3/2$. To examine whether the above explanation is acceptable, we define the "age" of the turbulence as the number N of nonlinear times t_{NL} accumulated since the beginning of the calculation. It can be expressed as

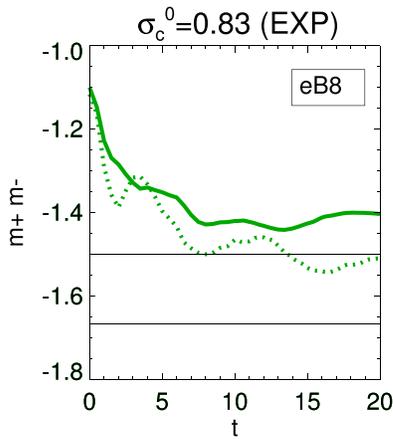$$N(t) = \int_0^t k_y^0(t')\, u_{rms}(t')\, dt', \qquad (18)$$

Figure 18. Evolution of spectral indices up to time $t = 20$, run $eB8$.

where k_y^0 and u_{rms} are, respectively, the smallest wavenumber and the rms velocity fluctuation.

The age versus time is shown in Figure 19 for four runs with large cross helicity without and with expansion: $hA8$, $hB8$, $eA8$, and $eB8$ with black, blue, red, and green solid lines, respectively. The difference between the two homogeneous runs and the two runs with expansion is drastic. The two homogeneous runs have their age growing almost linearly with time, from $t = 0$ up to 10, due to (i) the constancy of the largest scale and (ii) the limited decay of the largest eddies with time. The two runs with expansion, on the contrary, show a quasi-saturation of their age after time $t \simeq 8$. This is due to both a higher-amplitude decay rate and the linear expansion of the plasma with time in the two directions transverse to radial $(1/k_y^0(t) \propto a = R/R_0 \propto 1 + \epsilon t$; Equation (6)).

To evaluate the relative importance of these two effects on the freezing, we plotted with dotted lines the age obtained when taking into account only the turbulence amplitude (i.e., replacing $k_y^0(t)$ with $k_y^0(t = 0)$) for runs $eA8$ and $eB8$. The resulting curves show a decrease compared to the two curves for homogeneous runs but clearly do not correspond to a saturation of the age. One may thus conclude that the main origin of the quasi-freezing of the spectral evolution is due principally to the expansion of the largest eddies and secondarily to the indirect effect of expansion, which is the increased decay of the turbulent amplitude.

Note that in the simple, nonturbulent case of the shock formation of an acoustic wave with a wavevector lying within the perpendicular plane, one analytically finds that the increase of the effective expansion, when initially large enough, stops the wave from steepening before the shock is formed (Grappin et al. 1993).

5. Conclusion

In this paper, we considered decaying turbulence, starting with random fluctuations of velocity and magnetic field, and varying initial cross helicity and spectral index. Our key results can be summarized as follows (we denote results obtained using homogeneous runs with (H) and results obtained using runs with expansion with (E)).

1. The $m_{\pm}$ indices converge to values independent of the initial conditions (H); on the contrary, the indices keep a memory of the initial conditions (E).
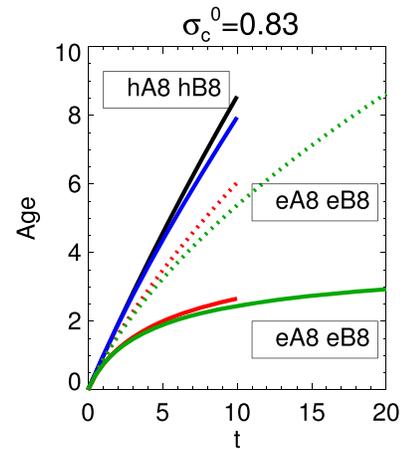

Figure 19. Age of turbulence for four runs with cross helicity $\sigma_c^0 = 0.83$. Run $hA8$ is black, $hB8$ blue, $eA8$ red, and $eB8$ green. Solid lines correspond to age defined as in Equation (18), and dotted lines correspond to replacing wavenumber $k_y^0(t)$ with its initial value in Equation (18), i.e., not taking expansion into account in the age evaluation.

2. Pinning occurs with nonzero σ_c^0; as a result, $|m_+|/|m_-|$ relaxes to a value that grows with σ_c^0 (H). On the contrary, as a rule, $m_+ \simeq m_-$, probably due to a permanent injection of the subdominant mode E_- at the largest scale by expansion (E).

3. The memory of initial conditions allows one to understand the conservation of the correlation between high cross helicity and flat spectra during the transport between 0.2 and 1 au, but the generation of the correlation probably occurs close to the Sun, requiring physical effects that are absent from the present simulations (E).

4. When increasing B_0, pinning persists, but both $E_{\pm}$ spectra steepen, as already known in the $\sigma_c^0 = 0$ case (H). Some pinning appears, and the spectra also steepen (E).

It would be interesting in future work to consider smaller values of the expansion parameter in order to be directly applicable to the inertial range. Also, increasing the resolution would allow one to describe the break separating the large-scale $1/f$ range from the true inertial range.

ORCID iDs

Roland Grappin ⓘ https://orcid.org/0000-0001-7847-3586

References

Adhikari, L., Zank, G. P., Zhao, L. L., et al. 2020, ApJS, 246, 38
Bavassano, B., & Bruno, R. 1995, JGR, 100, 9475
Bavassano, B., Dobrowolny, M., Mariani, F., & Ness, N. F. 1982, JGR, 87, 3617
Bavassano, B., Pietropaolo, E., & Bruno, R. 2000, JGR, 105, 15959
Bavassano, B., Pietropaolo, E., & Bruno, R. 2002, JGR, 107, 1452
Boldyrev, S. 2005, ApJL, 626, L37
Boldyrev, S., Perez, J. C., Borovsky, J. E., & Podesta, J. J. 2011, ApJL, 741, L19

Chandran, B. D. G., Dennis, T. J., Quataert, E., & Bale, S. D. 2011, ApJ, 743, 197
Chandran, B. D. G., Schekochihin, A. A., & Mallet, A. 2015, ApJ, 807, 1
Chen, C., Bale, S., Bonnell, J. W., et al. 2020, ApJS, 246, 53
Chen, C., Bale, S., Salem, C. S., & Maruca, B. A. 2013, ApJ, 770, 125
Chen, C., Mallet, A., Schekochihin, A. A., et al. 2012, ApJ, 758, 120
Cranmer, S. R., van Ballegooijen, A. A., & Edgar, R. J. 2007, ApJS, 171, 520
Dmitruk, P., Gomez, D. O., & Matthaeus, W. H. 2003, PhPl, 10, 3584
Dobrowolny, M., Mangeney, A., & Veltri, P. 1980, PhRvL, 45, 144
Dong, Y., Verdini, A., & Grappin, R. 2014, ApJ, 793, 118
Grappin, R., Frisch, U., Pouquet, A. G., & Léorat, J. 1982, A&A, 105, 6
Grappin, R., Léorat, J., & Pouquet, A. G. 1983, A&A, 126, 51
Grappin, R., Mangeney, A., & Marsch, E. 1990, JGR, 95, 8197
Grappin, R., Velli, M., & Mangeney, A. 1991, AnGeo, 9, 416
Grappin, R., Velli, M., & Mangeney, A. 1993, PhRvL, 70, 2190
Horbury, T. S., Forman, M., & Oughton, S. 2008, PhRvL, 101, 175005
Lithwick, Y., & Goldreich, P. 2003, ApJ, 582, 1220
Lithwick, Y., Goldreich, P., & Sridhar, S. 2007, ApJ, 655, 269
Matsumoto, T. 2021, MNRAS, 500, 4779
Matthaeus, W. H., Goldstein, M. L., & Roberts, D. A. 1990, JGR, 95, 20673
Matthaeus, W. H., Klein, L. W., Ghosh, S., & Brown, M. R. 1991, JGR, 96, 5421
Matthaeus, W. H., & Montgomery, D. 1980, in Int. Conf. on Nonlinear Dynamics 357 (New York: New York Academy of Sciences), 203

Montagud-Camps, V., Grappin, R., & Verdini, A. 2018, ApJ, 853, 153
Montagud-Camps, V., Grappin, R., & Verdini, A. 2020, ApJ, 902, 34
Ofman, L. 2010, LRSP, 7, 4
Oughton, S., & Matthaeus, W. H. 1995, JGR, 100, 14783
Perez, J. C., & Boldyrev, S. 2008, ApJ, 672, L61
Perez, J. C., & Boldyrev, S. 2010, ApJL, 710, L63
Pouquet, A. G., Sulem, P., & Meneguzzi, M. 1988, PhFl, 31, 2635
Rappazzo, A. F., Velli, M., Einaudi, G., & Dahlburg, R. B. 2007, ApJ, 657, L47
Réville, V., Velli, M., Panasenco, O., et al. 2020, ApJS, 246, 24
Roberts, D. A., Ghosh, S., Goldstein, M. L., & Matthaeus, W. H. 1991, PhRvL, 67, 3741
Roberts, D. A., Goldstein, M. L., Klein, L. W., & Matthaeus, W. H. 1987, JGR, 92, 12023
Shoda, M., Suzuki, T. K., Asgari-Targhi, M., & Yokoyama, T. 2019, ApJL, 880, L2
Shoda, M., Yokoyama, T., & Suzuki, T. K. 2018, ApJ, 853, 190
Squire, J., Chandran, B. D. G., & Meyrand, R. 2020, ApJL, 891, L2
van der Holst, B., Sokolov, I. V., Meng, X., et al. 2014, ApJ, 782, 81
Verdini, A., & Grappin, R. 2015, ApJL, 808, L34
Verdini, A., & Grappin, R. 2016, ApJ, 831, 179
Verdini, A., Velli, M., Matthaeus, W. H., Oughton, S., & Dmitruk, P. 2010, ApJL, 708, L116
Zhou, Y., & Matthaeus, W. H. 1990, JGR, 95, 10291